Available online at www.sciencedirect.com
ScienceDirect
Trans. Nonferrous Met. Soc. China 35(2025) 2886−2902
Transactions of Nonferrous Metals Society of China
www.tnmsc.cn

ZM51 magnesium alloy joint with high strength and thermal conductivity fabricated via friction stir welding and aging

Xu ZHANG[1,2], Zhi WANG[1,2], Feng-ming QIANG[1,2], Wen WANG[1,2], Peng HAN[1,2], Ting ZHANG[1,2], Qiang LIU[1,2], Yi LIU[1,2], Ke-yue HUO[1,2], Kuai-she WANG[1,2], Ke QIAO[1,2]

1. School of Metallurgical Engineering, Xi'an University of Architecture and Technology, Xi'an 710055, China;
2. National and Local Joint Engineering Research Center for Functional Materials Processing, Xi'an 710055, China

Received 8 January 2024; accepted 1 July 2024

Abstract: A ZM51 magnesium alloy joint with high intensity and thermal conductivity was fabricated using friction stir welding (FSW) followed by aging heat treatment (AG). During the FSW process, β_1' and β_2' phases formed in the heat-affected zone (HAZ), yet new phases were absent in both the stirring zone (SZ) and thermal mechanical affected zone (TMAZ). After AG, numerous β_1' and β_2' phases emerged in the SZ and the TMAZ of the joint, while only the β_2' phase precipitated in the HAZ. Due to precipitation strengthening, the average microhardness, yield strength and ultimate tensile strength of the joint reached up to 98%, 94% and 88% those of the base metal (BM), respectively. Notably, basal slip $\{0001\}\langle 11\bar{2}0\rangle$, and twinning at $60°/\langle 10\bar{1}0\rangle$ and $86°/\langle 11\bar{2}0\rangle$ were more prevalent in TMAZ, contributing to the joint's fracture. Furthermore, the precipitation of β_1' and β_2' phases enhanced the joint's thermal conductivity, averaging 121.7 W/(m·K), being 112% that of BM.

Key words: friction stir welding; ZM51 magnesium alloy; precipitated phase; tensile property; thermal conductivity

1 Introduction

Owing to their low density, high specific strength, and superior thermal conductivity [1,2], magnesium (Mg) alloys have gained increasing attention and are widely used in various fields, including household products, automotive electronics, and digital devices [3,4]. Mg alloys with high thermal conductivity are frequently shaped into complex components for specific applications. However, the hexagonal close-packed (HCP) structure of Mg alloys results in limited slip systems and reduced plastic deformation capacity. Consequently, processing Mg alloys through plasticity-forming methods, such as die forging, presents significant challenges.

Welding serves as a reliable method for processing Mg alloy components with complex structures. Traditional fusion welding techniques, including laser welding [5,6], fusion spot welding [7,8], and inert gas-shielded welding [9], are commonly employed. However, it is crucial to note that excessive heat input during fusion welding can lead to various solidification defects in Mg alloy welded joints, such as coarse grains, porosities, impurities, and thermal cracks, adversely affecting mechanical performance. Fusion welding of Mg alloy typically results in a significant grain coarsening, with grain sizes reaching up to 800 μm. This leads to a marked reduction in tensile strength, often only 60% that of the base metal (BM) [10]. Furthermore, ZHAO et al [11] reported a sharp decline in the thermal conductivity of Mg alloys

Corresponding author: Feng-ming QIANG, Tel: +86-15667089380, E-mail: qiangfengming@126.com;
Wen WANG, Tel: +86-13720527194, E-mail: wangwen2025@126.com
https://doi.org/10.1016/S1003-6326(25)66855-5

with an increase in the solidification defects. Consequently, the development of new welding methods is imperative to achieve defect-free joints, thereby ensuring Mg alloys to retain desirable mechanical properties and thermal conductivity.

Friction stir welding (FSW), a solid-phase welding technique, was developed by the Welding Institute in the UK [12]. Unlike fusion welding, FSW effectively avoids defects such as porosities and impurities, as the metal does not melt during the process [13−15]. FSW technology has been applied to Mg alloys. For instance, XU et al [16] utilized forced cooling FSW to weld AZ61 Mg alloy, achieving grain refinement in the nugget zone with an average grain size of 4.9 μm. The yield strength (YS) and ultimate tensile strength (UTS) of the joint increased by 16% and 6%, respectively, compared to those of the base metal (BM). Additionally, MOIDUDDIN et al [17] conducted high-strength welding of MgY_4Gd_3 alloy using FSW, where the joint's ultimate tensile strength coefficient exceeded 90%. It is noteworthy that the β-$Mg_{17}Al_{12}$ phase typically dissolves into the Mg matrix during the FSW, which can lead to a deterioration in the mechanical properties of the joint [18]. To address this issue, post-welding aging heat treatment (AG) was recommended [19,20].

This study examines the balance between mechanical properties and thermal conductivity in ZM51 (Mg−5wt.%Zn−1wt.%Mn) alloy joints, processed via FSW and subsequent AG. The emphasis lies in characterizing the joint's microstructure, mechanical properties, and thermal conductivity, specifically analyzing how the microstructure affects the mechanical and thermal conductivity properties of the FSW joint. This study aims to provide theoretical guidance for understanding the microstructural evolution, mechanical properties, and thermal conductivity of heat-conductive magnesium alloys during welding, to achieve high-quality connections in conductive magnesium alloys.

2 Experimental

2.1 FSW experiment

The extruded ZM51 sheet, sized at 120 mm × 40 mm × 3 mm, was welded on a FSW machine (FSW-LM-BM16). Weld speed and rotation speed were set at 100 mm/min and 1600 r/min, respectively. The cylindrical stir tool, constructed from H13 steel, had shoulder and pin diameters of 12 and 5 mm, respectively, with a pin length of 2.7 mm. During FSW, the tool was tilted by approximately 2.7°, and the plunge depth was maintained at 0.3 mm. Subsequently, the ZM51 joint underwent AG at 176 °C for 36 h in an argon environment, followed by furnace cooling to room temperature. Figure 1(a) depicts the FSW process schematic and the location for microstructure characterization sampling.

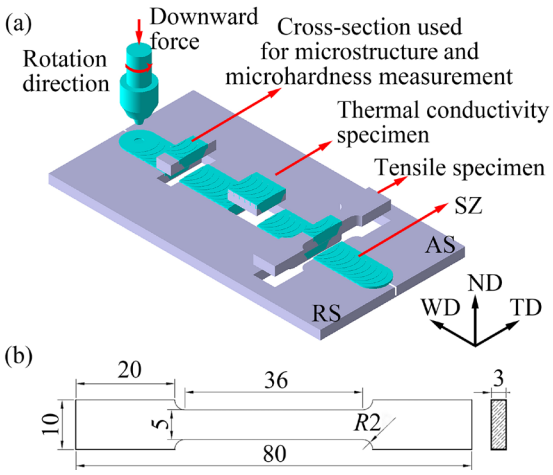

Fig. 1 (a) Schematic diagram of FSW process and sampling positions; (b) Dimensions of tensile specimen (WD, TD, and ND represent welding, transverse and normal directions, respectively; AS and RS represent advancing and retreating sides, respectively) (Unit: mm)

2.2 Microstructural characterization

Samples for microstructural characterization were sectioned perpendicularly to the WD. These samples underwent grinding, polishing, and etching for detailed microstructural analysis. The etchant comprised 3 vol.% picric acid, 4 vol.% acetic acid, 86 vol.% ethanol, and 7 vol.% water. Macroscopic and microscopic structures were examined using an optical microscope (OM, DP12) and a scanning electron microscope (SEM, Zeiss Gemini SEM 300). For electron backscatter diffraction (EBSD) analysis, the samples were electropolished in a 10 vol.% $HClO_4$ + 90 vol.% ethanol solution at −30 °C and 15 kV. Nano-scaled microstructural and crystallographic features were investigated using a Talos F200s transmission electron microscope (TEM). TEM foils were thinned to a thickness of 0.05 mm using ion thinning with Gantan 695.

2.3 Mechanical property test

Microhardness and tensile specimens were sectioned perpendicularly to the WD, as illustrated in Fig. 1(a). Microhardness test was performed using a 401 MVD microhardness tester, applying a load of 200 g, with a dwell time of 10 s and an indentation spacing of 0.5 mm. The dimensions of the tensile specimens are depicted in Fig. 1(b). Room temperature tensile tests were conducted using an Instron 8801 tester at an initial strain rate of $1\times10^{-3}\ s^{-1}$. To ensure the reliability of the results, each experimental set was repeated at least three times. The tensile fracture surfaces and microstructures were examined using OM, SEM, and EBSD, respectively.

2.4 Thermal conductivity test

The samples for the thermal conductivity test were sectioned perpendicularly to the WD, measuring 10 mm × 10 mm × 3 mm, as depicted in Fig. 1(a). The room temperature thermal diffusion coefficient was measured in an argon atmosphere utilizing the laser flash method [21]. The cross-sections of the joints (the sample surface perpendicular to the WD) were irradiated with a laser to measure the thermal conductivity of different regions of the joint. To ensure the precision of the results, each experimental set was replicated at least three times. The thermal conductivity (K) was calculated based on as follows [22].

$$K=\alpha\rho c_p \tag{1}$$

where α is the thermal diffusion coefficient; ρ is the density, which is measured using the drainage method; c_p is the specific heat capacity, which is calculated using the Neumann−Kopp rule [23].

3 Results

3.1 Microstructure of FSW joint

Figure 2 illustrates the cross-sectional macro-structure of the ZM51 FSW joint. From Fig. 2, it is evident that the joint is devoid of pores or cracks. The joint can be categorized into several zones based on morphological characteristics: the base metal (BM), stirring zone (SZ), thermal-mechanical affected zone (TMAZ), and heat-affected zone (HAZ). The SZ is characterized by a basin-shaped morphology, while the TMAZ is comparatively narrow. Additionally, no significant microstructural differences are observed between the retreating side (RS) and the advancing side (AS). Consequently, the RS of the ZM51 FSW joint was selected for detailed investigation of microstructure evolution in this study.

Figure 3 presents the EBSD micrographs of various regions in the FSW joint. As depicted in Fig. 3(a), the BM comprises predominantly long-strip shaped grains and some equiaxed grains, with an average size of 60 μm. In the SZ, as shown in Fig. 3(b), grains undergo severe plastic deformation and dynamic recrystallization due to the vigorous stirring action of the stirring pin [24]. This results in a refined equiaxed grain morphology with an average size of 9 μm. Fine grains will enhance the microhardness in this region [25,26]. The TMAZ, illustrated in Fig. 3(c), exhibits grains that are mechanically sheared and thermally influenced, leading to elongation along the metal flow direction. Dynamic recovery and recrystallization in the TMAZ refine the grains to an average size of 14 μm. Conversely, in HAZ, as shown in Fig. 3(d), grains are coarsened to an average size of 76 μm, attributed to thermal input.

In BM, the HAGBs (high-angle grain boundaries, >15°) accounted for 71.4%. Notably, a peak near 86° observed in Fig. 3(e) corresponds to the disorientation angle of $\{10\bar{1}2\}\langle10\bar{1}1\rangle$ twin, indicating a minor presence of tensile twins in BM [27]. The HAGBs proportion in the SZ was elevated to 76.2% (Fig. 3(f)), and in the TMAZ, it was 70.2% (Fig. 3(g)). Both the SZ and TMAZ underwent continuous dynamic recrystallization, with strong shear deformation leading to the generation of numerous dislocations in the original grains. These dislocations rearranged to form dislocation cells, which transformed into LAGBs

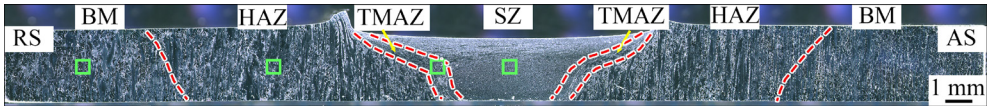

Fig. 2 Cross-sectional macrostructure of FSW joint (The green rectangle indicates the measurement positions for EBSD in each region)

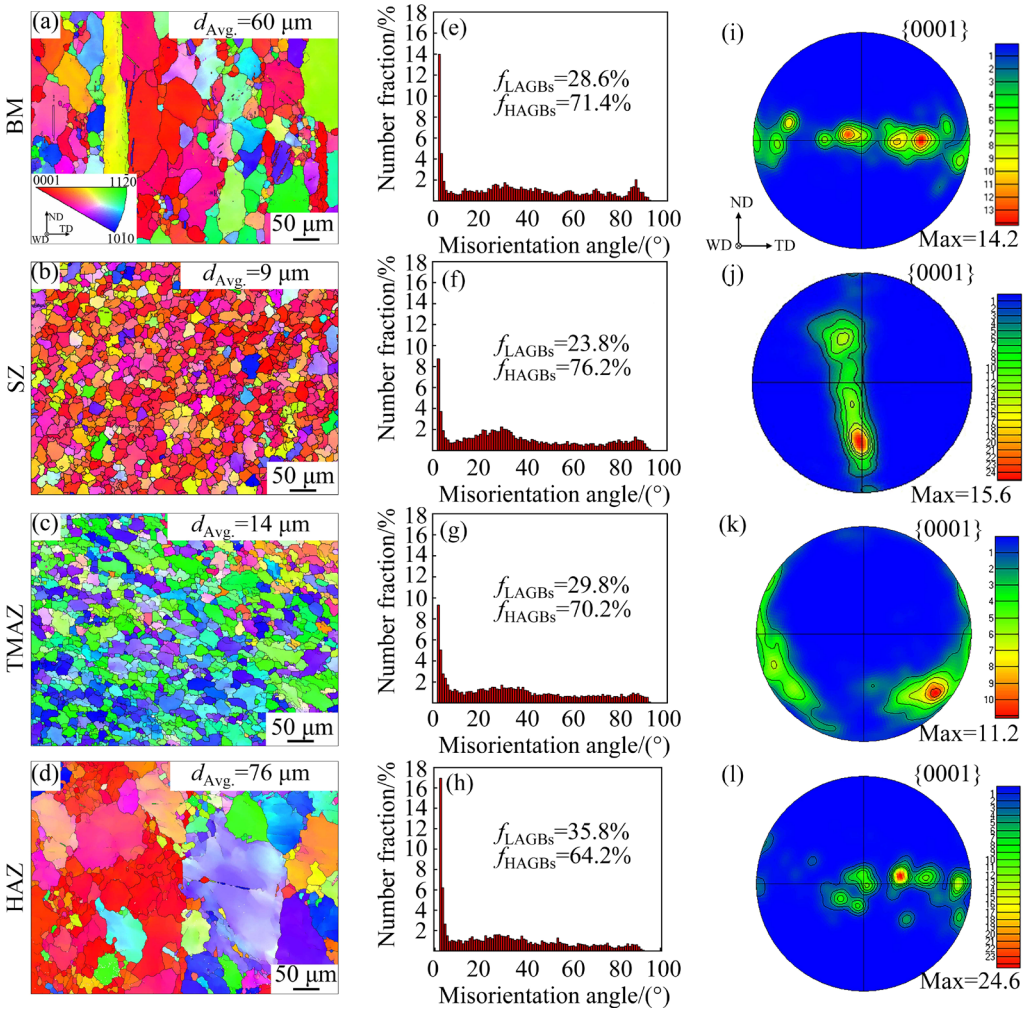

Fig. 3 EBSD micrographs of different regions (outlined with green rectangles in Fig. 2) in FSW joint: (a−d) Inverse pole figures; (e−h) Misorientation angle distribution; (i−l) Pole figures ($d_{Avg.}$ is the average grain size)

(low-angle grain boundaries, 2°−15°) and eventually evolved into HAGBs. Conversely, the HAGBs proportion in the HAZ decreased to 64.2% (Fig. 3(h)), attributed to thermal effects where some grains grew and absorbed neighboring grains, reducing the HAGBs proportion.

Furthermore, texture significantly influences the properties of Mg alloy joints [27], and hence, the texture distribution was analyzed using EBSD, as presented in Figs. 3(i−l). BM exhibited a typical fiber texture ({0001}//ND) with a maximum polar density of 14.2 (Fig. 3(i)). After the FSW, grains in the SZ showed the *c*-axis deviating from the TD by 86°−90° (Fig. 3(j)). In TMAZ, the *c*-axis of grains deviated from TD by 40°−43° (70°−76° from WD) (Fig. 3(k)). In HAZ, the deviation was 30°−35° from TD (55°−60° from WD) (Fig. 3(l)). This texture evolution is correlated closely with material flow during the FSW [28]. As the material flows around the stir pin's surface due to the rotating force, the (0001) basal plane in the welding zone aligns approximately parallel to the stir pin's surface. Consequently, the rotation of the stirring pin induces a shift in the basal plane, causing the *c*-axis of grains from the SZ to the HAZ to increasingly deviate from WD to TD.

The nano-scaled microstructural characteristics of each area within the FSW joint are visualized via STEM and depicted in Fig. 4. As indicated by blue arrows in Fig. 4(a), spherical and rod-shaped precipitates are dispersed in the BM, confirmed by EDS elemental mapping (Fig. 4(a_1)) as α-Mn. The orientation relationship between α-Mn and the matrix is identified as $(11\bar{2}0)_{\alpha\text{-Mg}}//(001)_{\alpha\text{-Mn}}$ and $[0001]_{\alpha\text{-Mg}}//[111]_{\alpha\text{-Mn}}$ [29]. In the SZ, the morphology of the α-Mn phase remains similar to

that of BM, albeit with reduced content, likely due to phase dissolution during the FSW (Fig. 4(b)). In the TMAZ, the morphology and quantity of the α-Mn phase mirror those in BM (Fig. 4(c)). Conversely, in the HAZ, the α-Mn phase content is significantly diminished, and other fine precipitates emerge (inset in Fig. 4(d)). This change is attributed to thermal cycling effects in the HAZ, which promote phase dissolution and subsequent precipitation. EDS analysis results of these fine precipitates in the HAZ are shown in Fig. 4(d_1), revealing the enrichment in Mg and Zn, indicative of the $MgZn_2$ phase [30]. This phase manifests as rod-shaped β_1' and disc-shaped β_2' phases, each exhibiting distinct orientation relationships with the Mg matrix. β_1' phase is coherent with the Mg matrix (Fig. 5(a)), and the orientation relationship is as follows: $(01\bar{1}0)_{\alpha\text{-Mg}}//(01\bar{1}0)_{MgZn_2}$ and $[\bar{2}110]_{\alpha\text{-Mg}}//[0001]_{MgZn_2}$. Meanwhile, β_2' phase is semi-coherent with the Mg matrix (Fig. 5(b)), adhering to the relationship: $(2\bar{1}\bar{1}0)_{\alpha\text{-Mg}}//(\bar{1}010)_{MgZn_2}$ and $[0001]_{\alpha\text{-Mg}}//[0001]_{MgZn_2}$.

3.2 Microstructure of FSW joint after AG

Figure 6 illustrates the microstructure of the FSW joint following aging heat treatment (FSW+AG). The average grain sizes in BM, SZ, TMAZ, and HAZ were measured as 85, 16, 17, and 78 μm,

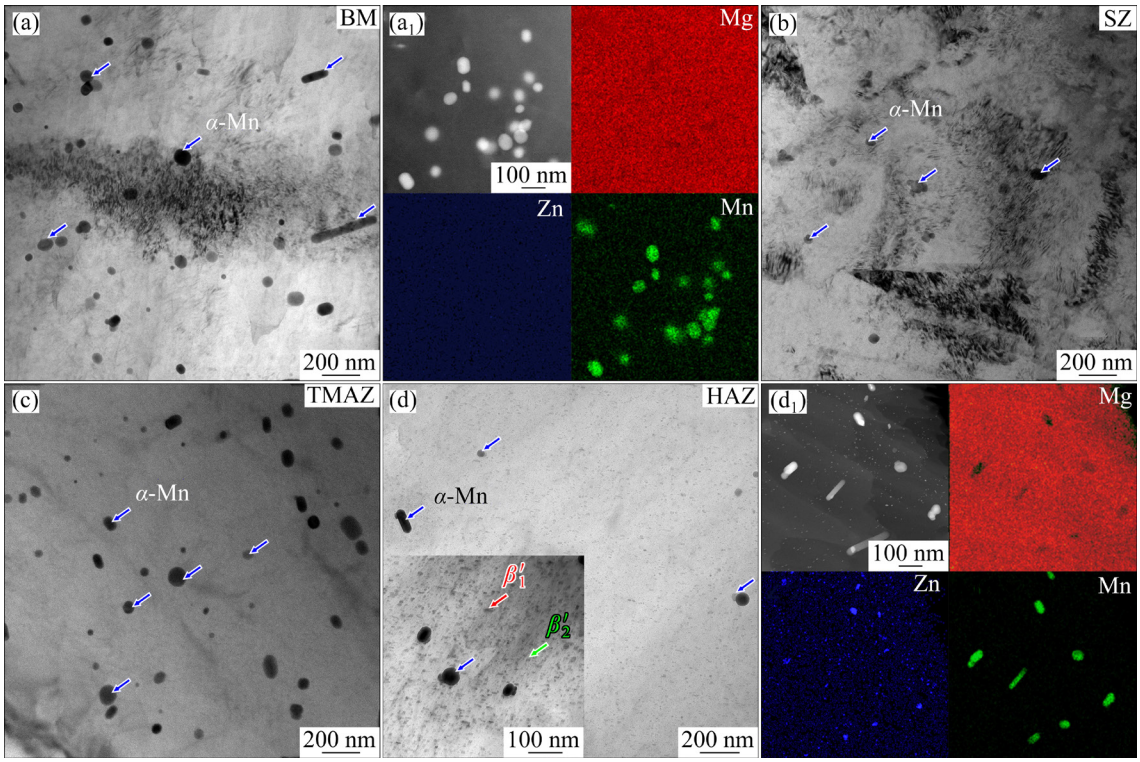

Fig. 4 Scanning transmission electron microscope (STEM) images of FSWed ZM51 joint: (a−d) Bright field TEM (BF-TEM) images of BM, SZ, TMAZ, and HAZ, respectively; (a_1) EDS map of BM; (d_1) EDS map of HAZ

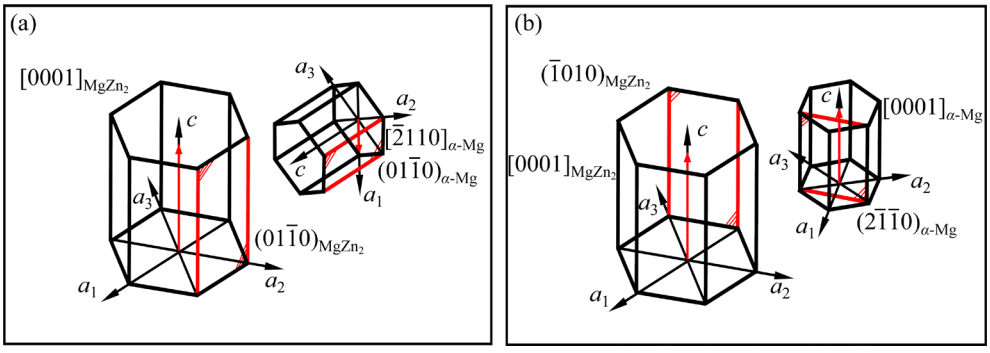

Fig. 5 Orientation relationship between precipitated phases with Mg matrix: (a) β_1' phase; (b) β_2' phase

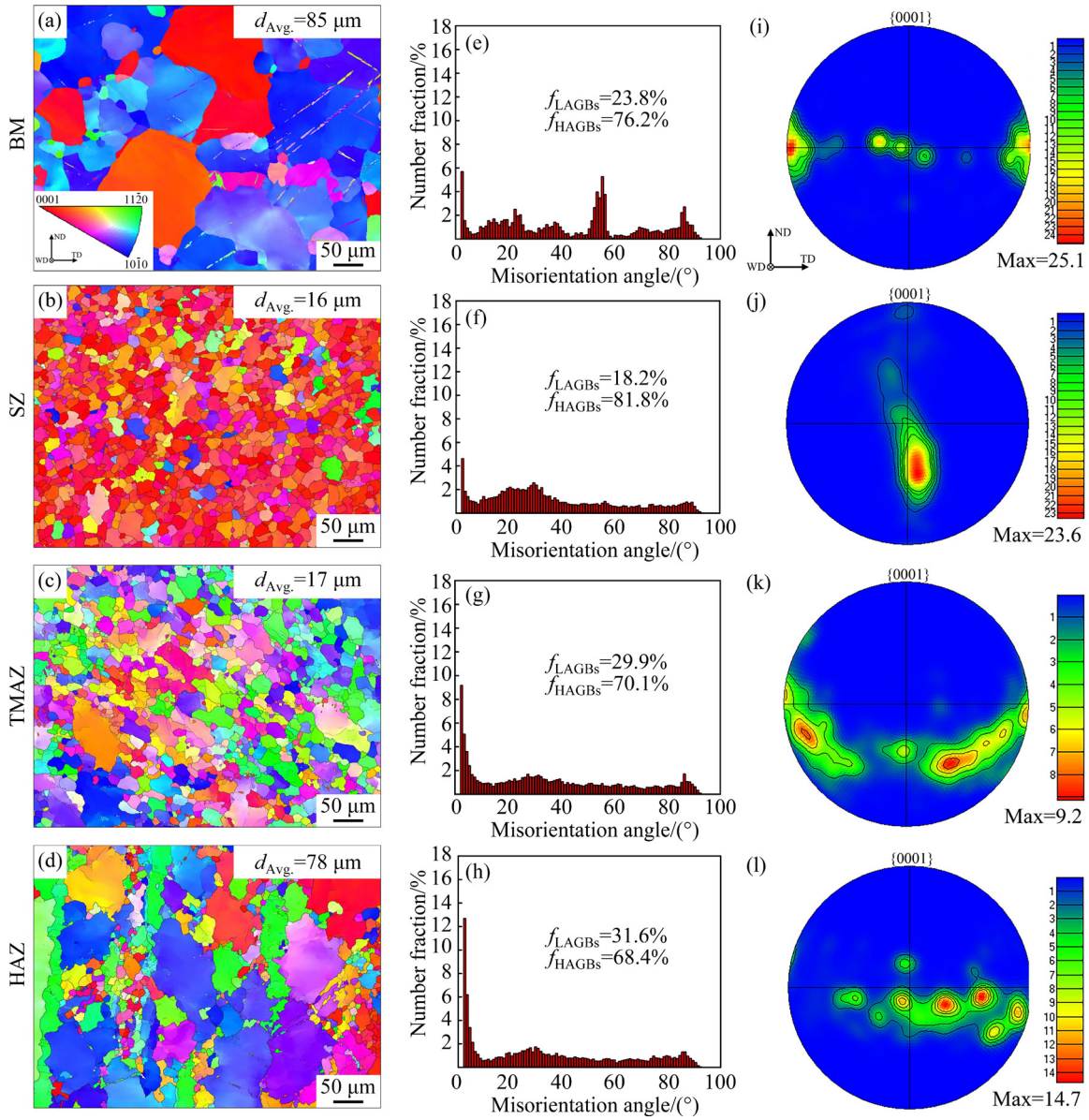

Fig. 6 EBSD micrographs of different regions in FSW joint after AG: (a−d) Inverse pole figures; (e−h) Misorientation angle distribution; (i−l) Pole figures

respectively (Figs. 6(a−d)). It is observed that during AG, grain growth occurred, albeit without severe coarsening. Additionally, the proportion of HAGBs in the FSW joint, encompassing BM, SZ, and HAZ, increased (Figs. 6(e, f, h)). This increment is attributed to static recrystallization (SRX) occurring during AG, which facilitates the transition from low-angle grain boundaries (LAGBs) to HAGBs. Moreover, the texture in each region of the FSW+AG joint closely resembles that of the FSW joint (Figs. 6(i−l)), indicating that AG does not significantly alter the texture evolution in the FSW joint.

Figure 7 displays the STEM images of the FSW+AG joint, clearly revealing an abundance of precipitates in BM, SZ, TMAZ, and HAZ (Figs. 7(a−d)). The EDS analysis (Figs. 7(e−h)) identifies these precipitates as α-Mn, β_1', and β_2' phases. In BM, along with α-Mn phase, a considerable number of rod-shaped and disc-shaped fine β_1' and β_2' phases are present (marked by red and green arrows, respectively, in Fig. 7(a)). In SZ and TMAZ, only β_1' and β_2' phases are observed, with β_2' phase being relatively scarce. In HAZ, β_1' phase is almost absent, and the precipitates primarily consist of α-Mn phase and a large quantity of β_2' phase (Fig. 7(d)). Previous study [31] suggested that β_2' phase can originate from the

matrix or evolve from β'_1 phase under extensive AG conditions. During the FSW process, the HAZ undergoes thermal input, leading to significant precipitation of β'_1 phase (Fig. 4(d)). Subsequent AG facilitates the transformation from β'_1 phase to β'_2 phase.

In conclusion, when compared to the original FSW joint, the AG results in a decrease in α-Mn phase content, while significantly increasing contents of β'_1 and β'_2 phases. This suggests that AG treatment promotes the dissolution of α-Mn phase and facilitates the precipitation of numerous rod-shaped and plate-shaped fine β'_1 and β'_2 phases.

3.3 Mechanical properties and thermal conductivity of joints

3.3.1 Hardness distribution

Figure 8 illustrates the microhardness distribution in FSW and FSW+AG joints. As depicted in Fig. 8(a), the microhardness distribution of the FSW joint is roughly symmetrical concerning the midline of the SZ, although fluctuation is noted in various areas. The highest microhardness is observed in BM (approximately HV 80), with the average microhardness values in SZ, TMAZ, and HAZ being HV 64, HV 62, and HV 65, respectively. These values are 20%, 23%, and 19% lower than that of BM. After AG, the FSW joint displays a more uniform microhardness distribution (Fig. 8(b)). The average microhardness values in SZ, TMAZ, and HAZ in the FSW+AG joint are HV 79, HV 76, and HV 80, respectively, representing increments of 23%, 22%, and 23% over the FSW joint and almost equating to BM levels. The enhancement in microhardness is primarily attributed to the precipitation strengthening effect of β'_1 and β'_2

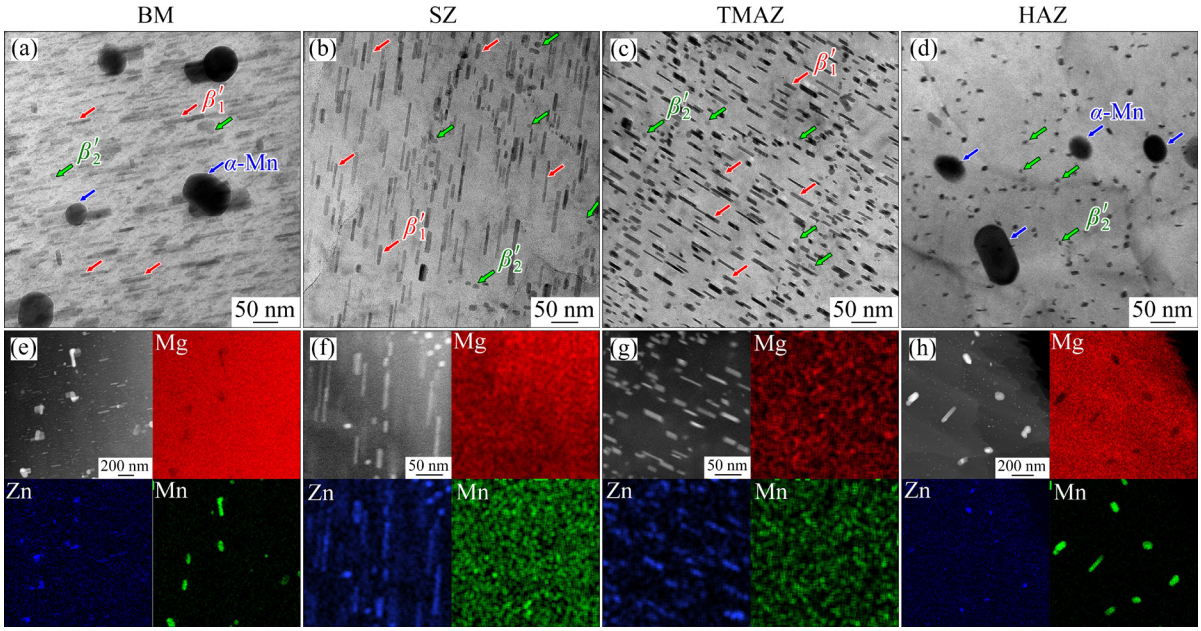

Fig. 7 STEM images of FSW+AG joint: (a−d) BF TEM images; (e−h) STEM EDS maps

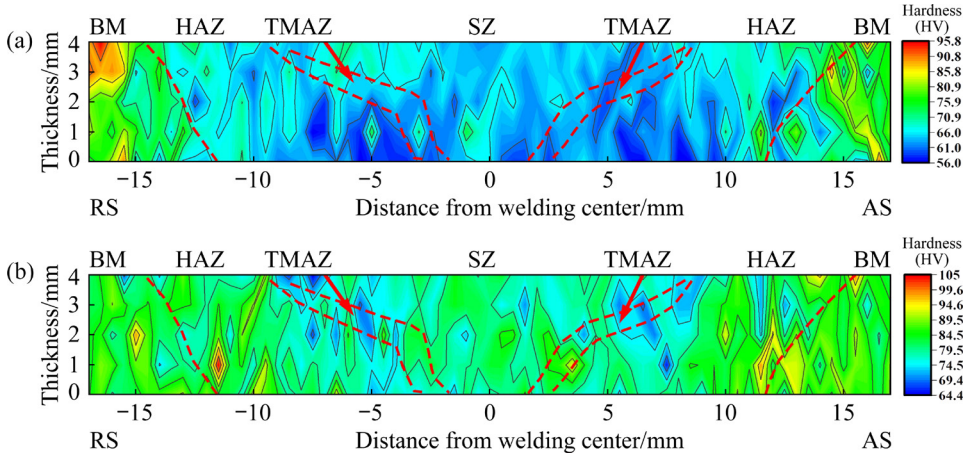

Fig. 8 Microhardness distribution on cross-section of different joints: (a) FSW joint; (b) FSW+AG joint

phases during the AG process. Notably, both FSW and FSW+AG joints exhibit the lowest micro-hardness in the TMAZ.

3.3.2 Tensile properties

Figure 9 presents the engineering stress−strain curves and ambient tensile properties of BM, and FSW and FSW+AG joints. The ultimate tensile strength (UTS), yield strength (YS), and elongation (EL) of BM are 298 MPa, 143 MPa, and 12.4%, respectively. For the FSW joint, the corresponding values are 255 MPa for UTS, 80 MPa for YS, and 13.9% for EL. After the AG treatment, the UTS and YS of the FSW+AG joint increased to 263 MPa and 135 MPa, respectively, while EL decreased to 6.9%. Compared to the FSW joint, the UTS and YS of the FSW+AG joint increased by 3% and 69%, respectively, primarily due to the precipitation strengthening effect of β_1' and β_2' phases. However, stress concentration around these precipitated phases during tensile testing promoted crack initiation and propagation, thereby reducing the EL of the FSW+AG joint [32]. Notably, the UTS and YS of the FSW+AG joint reached 88% and 94% those of the BM values, respectively, indicating a high joint efficiency.

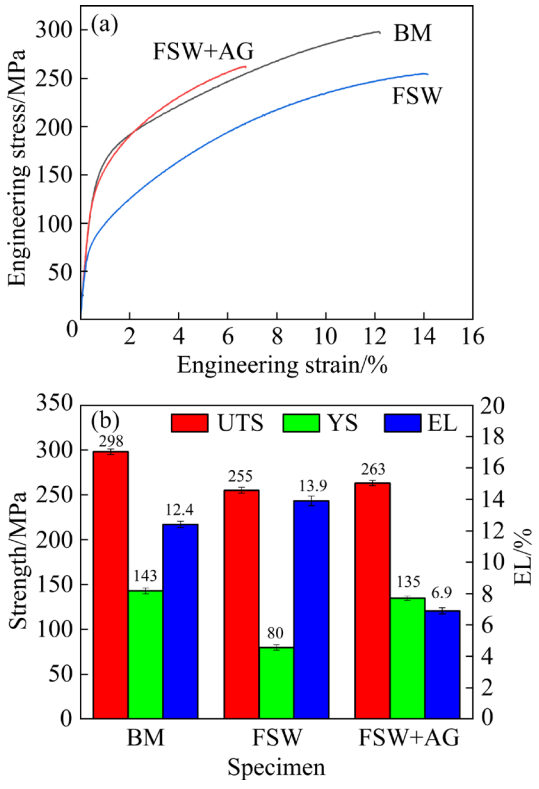

Fig. 9 Tensile test results of BM, and FSW and FSW+AG joints: (a) Engineering stress−strain curves; (b) Tensile properties

Figure 10 illustrates the fracture surface morphology of BM, and FSW and FSW+AG joints. The fracture surfaces of these joints exhibit a plethora of cleavage facets, tearing ridges, and dimples, indicative of mixed ductile−brittle fracture characteristics. It is noteworthy that the fracture surface of the FSW joint contains a significantly higher number of dimples compared to that of the FSW+AG joint, while the occurrences of tearing ridges and cleavage facets are reduced. This observation implies that the FSW joint shows superior ductility relative to the FSW+AG joint, aligning with the previously measured EL values.

Figure 11 displays the macrostructure of FSW and FSW+AG joints near the fracture location. It is evident that both FSW and FSW+AG joints

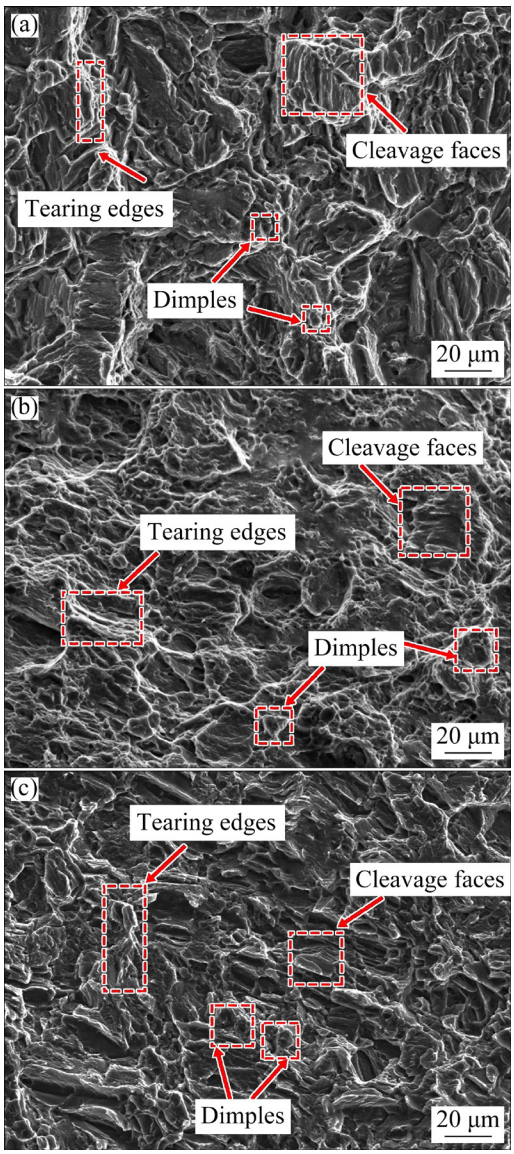

Fig. 10 Fracture surface morphologies of different samples: (a) BM; (b) FSW joint; (c) FSW+AG joint

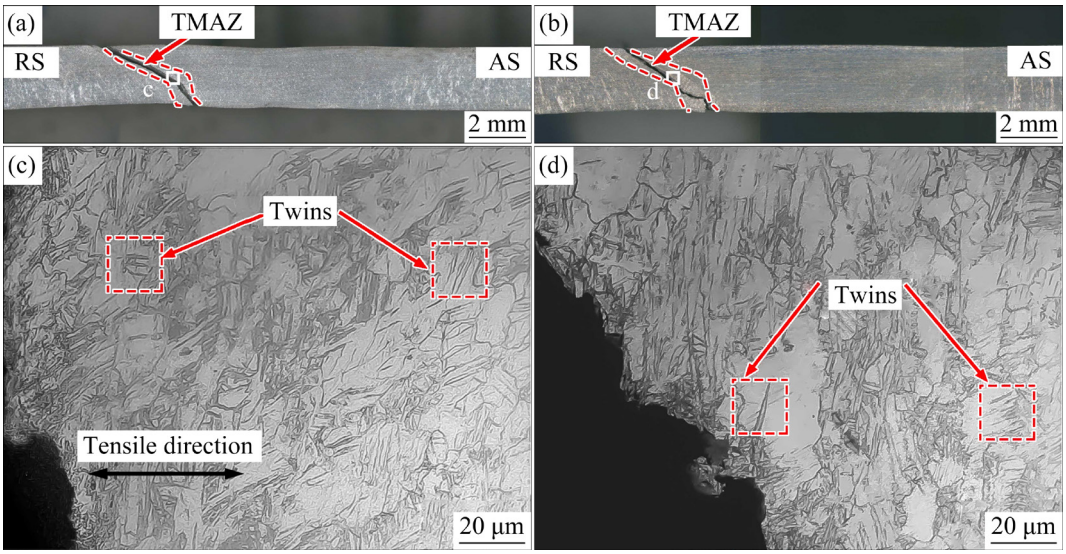

Fig. 11 Macro- and microstructures of joints after tensile tests: (a, b) Macroscopic fracture morphologies of FSW and FSW+AG joints, respectively; (c, d) Optical micrographs near fracture of FSW and FSW+AG joints, respectively

fractured in the TMAZ, as shown in Figs. 11(a, b). Close to the fracture location in both joints, a high density of twins is observed, exhibiting an orientation of approximately 45° relative to the tensile direction (Figs. 11(c, d)).

To further elucidate the fracture mechanism of the joint, an investigation into the microstructural characteristics near the fracture area was conducted. Figure 12 displays the EBSD orientation maps of the FSW specimen after tensile deformation. Figures 12(a, b) show the grain boundary micrograph and the corresponding misorientation angle distribution in the TMAZ of the specimen. Notably, numerous boundaries exhibit disorientation angles and axes of $60°/\langle 10\bar{1}0\rangle$ and $86°/\langle 11\bar{2}0\rangle$, corresponding to $\{10\bar{1}2\}-\{10\bar{1}2\}$ secondary twinning and $\{10\bar{1}2\}$ extension twinning, respectively [33]. However, twin boundaries are nearly absent in the SZ (Figs. 12(c, d)) and HAZ (Figs. 12(e, f)). This absence is attributed to the smaller quantity of α-Mn phase in the SZ and HAZ, which diminishes its pinning effects on dislocations and hinders the achievement of the critical resolved shear stress (CRSS) necessary for twin initiation. Conversely, the TMAZ, exhibiting a substantial accumulation of α-Mn phase (Fig. 4(c)), shows a pronounced tendency for twinning. Therefore, it can be concluded that twinning is more likely to occur in the TMAZ than in the SZ during tensile deformation, leading to twinning deformation predominantly concentrated in the TMAZ.

Furthermore, the activation of slip mechanisms in Mg alloys plays a crucial role in their deformation behavior [34]. Typically, the most readily activated slip system in Mg alloys is the basal slip, while prismatic and pyramidal slip systems require higher CRSS at room temperature [35,36]. To further explore the deformation behavior in different regions of FSW and FSW+AG joints, Fig. 13 presents the Schmid factor (SF) maps for basal slip $\{0001\}\langle 11\bar{2}0\rangle$ in the SZ, TMAZ, and HAZ along the TD before tensile deformation. In both FSW and FSW+AG joints, the SF maps of the SZ predominantly display blue and green colors, corresponding to average SF values of 0.21 and 0.22, respectively. In contrast, the TMAZ shows extensive areas of red and yellow, with only a few regions being blue, leading to average SF values of 0.38 and 0.34, respectively. The average SF value in the HAZ lies between those of the SZ and TMAZ. Notably, the TMAZ exhibits the highest average SF value for basal slip, suggesting that slip deformation is more likely to initiate in the TMAZ of the joint.

In summary, the dominant deformation mechanisms in FSW and FSW+AG specimens are identified as twinning and basal slip. The localized strain within the joint, resulting from the differential activation of these deformation mechanisms, is a key contributor to joint failure. During tensile loading, the TMAZ actively facilitates the initiation of twinning and basal plane slip. Throughout tensile

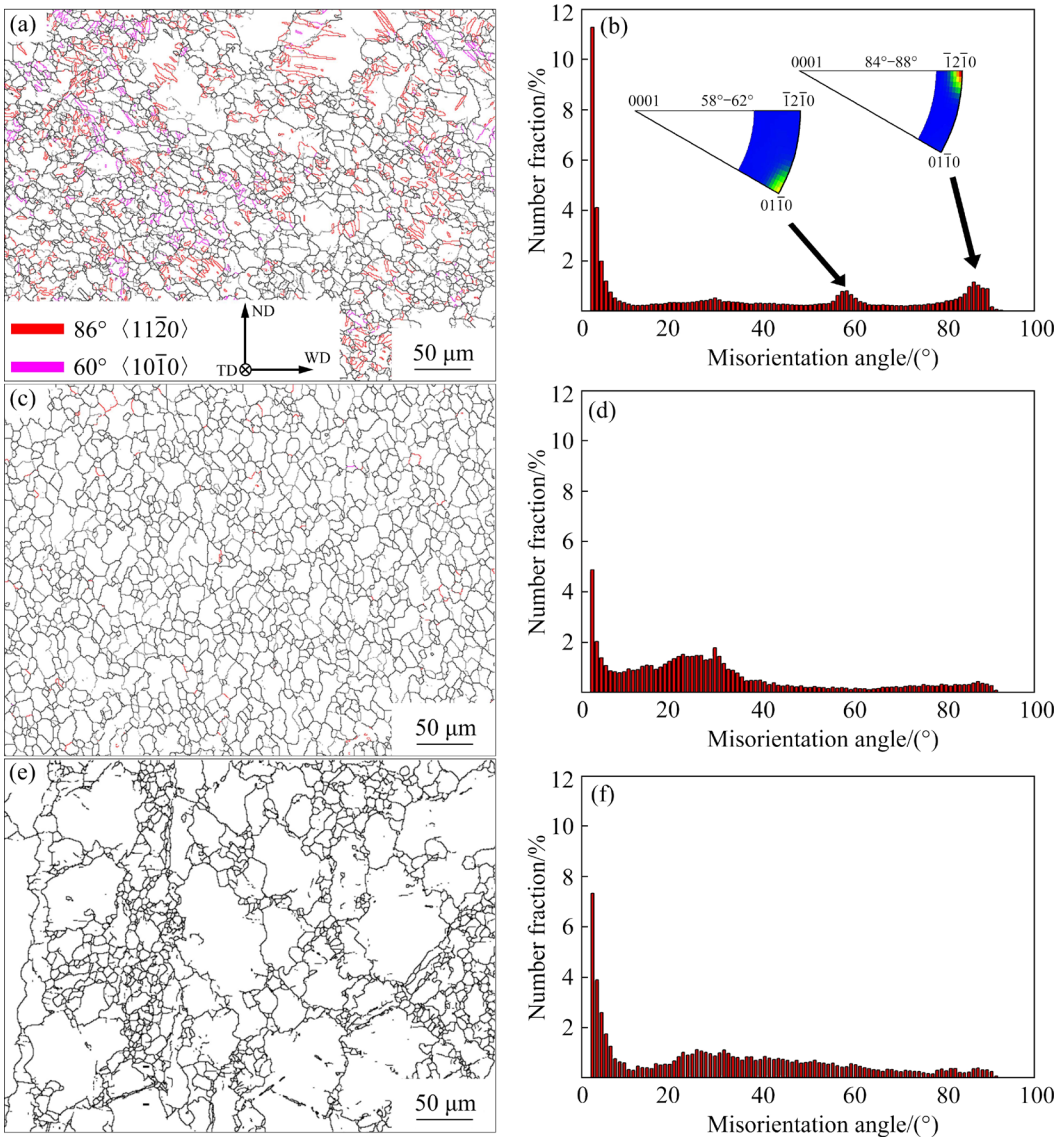

Fig. 12 EBSD orientation maps of FSW specimen after tensile deformation: (a, c, e) Grain boundary micrographs in TMAZ, SZ and HAZ of FSW joint, respectively; (b, d, f) Misorientation angle distribution in (a), (c) and (e), respectively

deformation, micro-cracks are observed to initiate at grain boundaries, subsequently propagating and experiencing deflection along twin boundaries [37]. Regions experiencing high stress and crack formation are particularly prone to occur at intersections of twin boundaries, ultimately leading to the fracture of the specimen.

3.3.3 Thermal conductivity

Figure 14 presents the thermal conductivity statistics of FSW and FSW+AG joints, excluding the TMAZ due to its minimal area. The thermal conductivity in the FSW joint is observed to be 108.3 W/(m·K) for the BM, 104.8 W/(m·K) for the SZ, and 114.2 W/(m·K) for the HAZ. Notably, there is significant fluctuation in thermal conductivity across different regions of the joint, with SZ exhibiting a thermal conductivity that is 9.4 W/(m·K) lower than that of the HAZ. This indicates a non-uniform thermal conductivity within the joint. In comparison, the thermal conductivity in the FSW+AG joint shows an increase to 121.4 W/(m·K) for the BM and SZ, and 122.2 W/(m·K) for the HAZ. These results suggest that AG treatment not only improves the overall thermal conductivity of the ZM51 Mg alloy welded joint but also contributes to a more uniform thermal conductivity distribution across different regions of the joint.

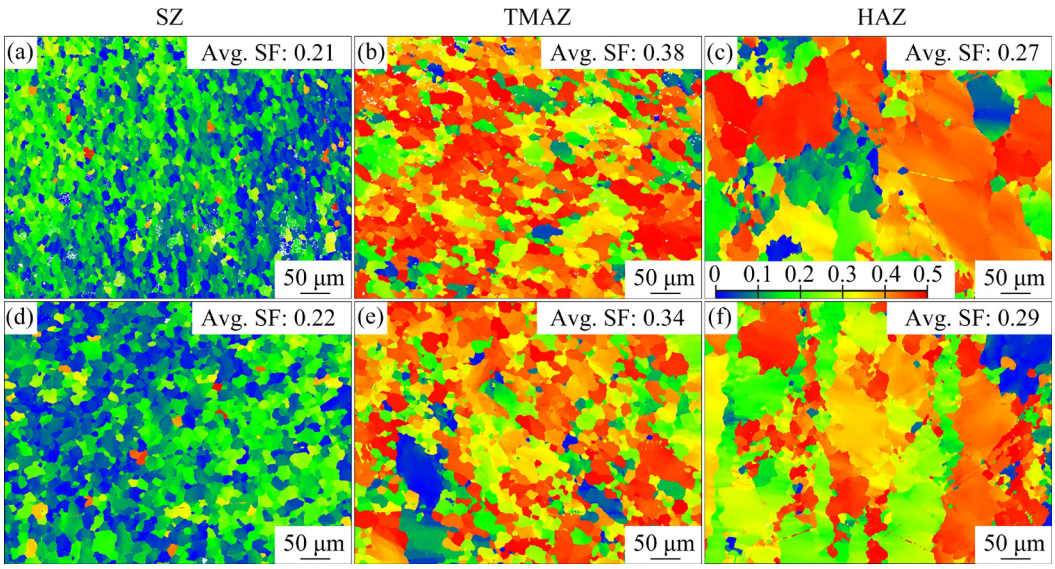

Fig. 13 SF maps of $\{0001\}\langle 11\bar{2}0\rangle$ basal slip in various regions of FSW and FSW+AG joints along TD: (a−c) FSW joint; (d−f) FSW+AG joint

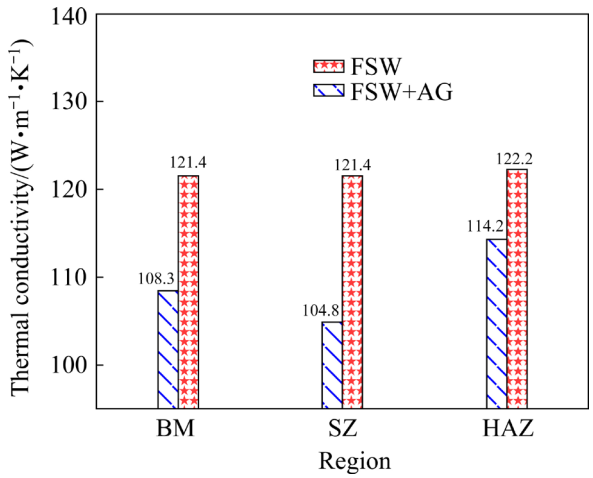

Fig. 14 Thermal conductivity of different regions in FSW and FSW+AG joints

4 Discussion

4.1 Effect of FSW and AG on microstructure and mechanical properties

4.1.1 FSW joint

The mechanical properties of a material are intimately linked to its microstructure. In this study, it was observed that the mechanical properties were significantly influenced by the precipitation phase, grain size, and texture structure [38]. A significant amount of α-Mn phase is present in the BM. A quantitative analysis of α-Mn phase size in both the BM and the joint was carried out, and the results are displayed in Fig. 15. In the SZ and TMAZ, α-Mn phases with diameters ranging from 10 to 30 nm make up 77% and 69% of the total, respectively. The average diameters of α-Mn phases in the SZ and TMAZ are 23.8 and 25.8 nm, respectively. The average diameter of α-Mn phase in the HAZ is 33.8 nm, which is significantly larger than that in the BM, indicating the coarsening of α-Mn phase. On the other hand, as shown in Fig. 4, the quantities of α-Mn phase in the SZ and the HAZ are significantly lower than that in the BM. While the quantity of α-Mn phase in the TMAZ is nearly equal to that in the BM. Typically, the smaller and the more the particles of the secondary phase are, the greater the strengthening effect providing to the magnesium matrix is [38]. However, as shown in Fig. 8, the microhardness of the TMAZ is lower than that of the SZ and HAZ, indicating that the influence of α-Mn phase on the microhardness is relatively low. ZHANG et al [39] explained that the main function of α-Mn phase is to serve as a heterogeneous nucleation site for new grains, which helps to refine the microstructure. Contrary to the Hall−Petch relationship, which posits that finer grains lead to higher microhardness [40], a decrease in microhardness was observed despite the FSW joints having significantly finer grains (Fig. 3). This suggests that the grain size is not the primary factor influencing the strength of ZM51 welded joints.

As depicted in the polar coordinate plots (Figs. 3(i−l)), the orientation of the FSW joint exhibits a significant deviation from that of BM. This difference primarily originated from the

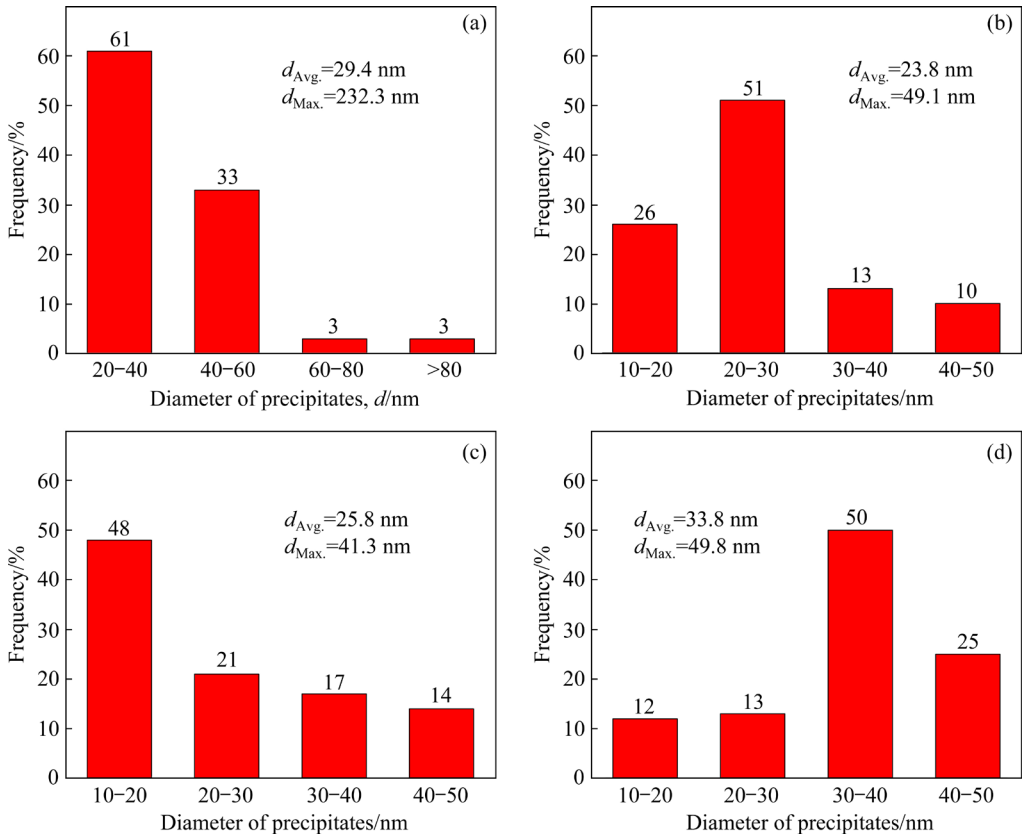

Fig. 15 Size distribution of α-Mn phase in different regions of welding joints: (a) BM; (b) SZ; (c) TMAZ; (d) HAZ

combined thermal input and shear forces during the FSW process, which altered the texture of the BM [41]. Specifically, in the TMAZ, the *c*-axis orientation changes between 40° and 43° relative to the TD, due to the combined effects of thermal input and shear forces during the FSW. This orientation lowers the CRSS for basal plane slip, making it more likely under tensile loads. The SF for basal plane slip in the TMAZ is 0.38, suggesting a heightened susceptibility to plastic deformation in this region. This particular orientation results in a pronounced softening effect, evidenced by a notable reduction in hardness within the TMAZ, as shown in Fig. 7(a). Consequently, this characteristic indicates the presence of a potential weak zone within the joint, which may become a locus for the fracture under tensile loading, as demonstrated in Fig. 11(a).

FSW has modified the basal texture of ZM51 alloy, resulting in a refined grain structure and the dissolution and precipitation of minor secondary phases. Furthermore, the alteration in the basal texture is identified as the primary factor contributing to the differences in mechanical properties observed between the FSW joint and the BM.

4.1.2 FSW+AG joint

AG does not significantly affect the grain size of the FSW joint, as the grains remained uniformly fine throughout. This indicates the enhanced thermal stability of the grains during the AG process. Furthermore, the texture in various regions of the FSW+AG joint resembles that of the FSW joint, suggesting that the AG process does not exert a substantial influence on the texture evolution within the FSW joint.

After AG, a large number of fine β'_1 phases and a smaller number of β'_2 phases precipitate in the SZ and TMAZ. β'_1 phase predominantly occurs within the range of 10−30 nm in the SZ, with an average length of 22.4 nm Fig. 16(a). In the TMAZ, this phase is smaller, and its average length is 17.1 nm Fig. 16(b). Notably, there are a number of β'_1 phases exceeding 50 nm in the SZ and TMAZ, with the largest ones surpassing 90 nm in length. The HAZ mainly presents β'_2 phase, which has an average radius of 2.2 nm Fig. 16(c). β'_2 phase is relatively uniform in size, with a maximum radius of only 6.1 nm. The small size and large quantity of β'_1 and β'_2 phases can effectively pin dislocations, thereby

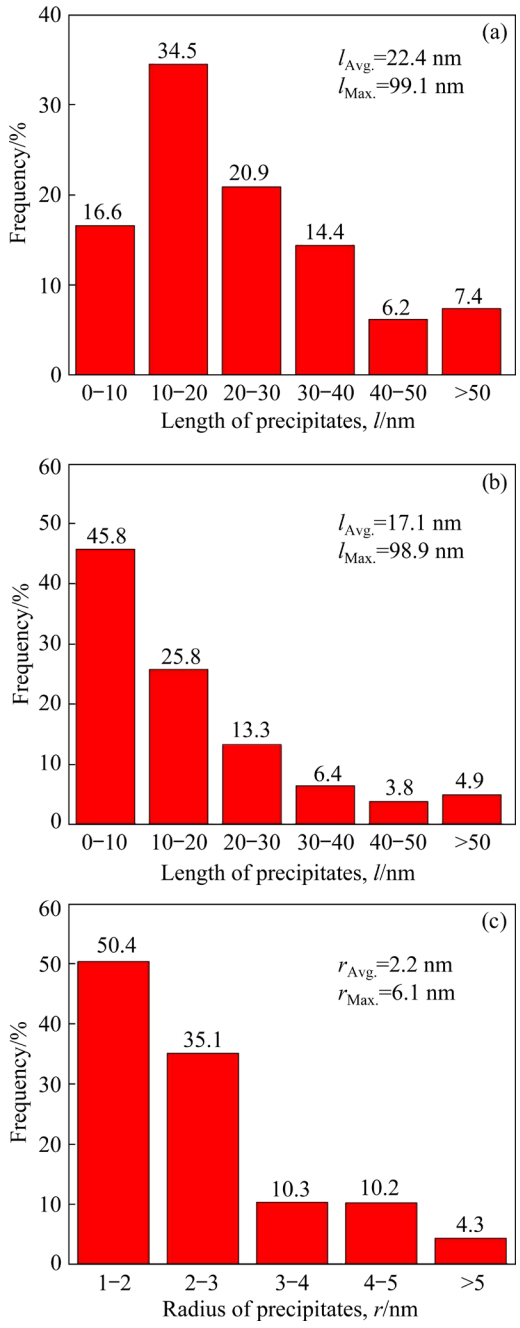

Fig. 16 Size distribution of β_1' phase in different regions of SZ (a) and TMAZ (b), and size distribution of β_2' phase in HAZ (c)

providing significant strengthening effects on the matrix. It is worth noting that some research suggests that β_1' phase is coherent with the matrix and offers a better strengthening effect than β_2' phase [42]. However, by comparing changes in microhardness values, this study has found that β_1' and β_2' phases contribute equally to the strengthening of the matrix. β_1' phase is distributed in the SZ and TMAZ, contributing to hardness increments of 23% and 22%, respectively. Similarly, β_2' phase in the HAZ also contributes to a hardness increment of 23%. The reason for this phenomenon is that some of β_1' phases are quite large (exceeding 90 nm) and the gaps between β'_1 phases are too wide, which diminishes their strengthening effect. In summary, the precipitated β_1' and β_1' phases after AG are the primary reasons for the increased strength and hardness of the joint.

4.2 Effect of FSW and AG on thermal conductivity

4.2.1 FSW joint

Research indicates that electrons and phonons are the primary media for heat transfer in alloys, and the thermal conductivity of magnesium alloys is determined by the mean free paths of heat transfer electrons and phonons. The thermal conductivity is directly proportional to the phonons' heat capacity and their mean free paths [43].

Firstly, the increase in solute atoms causes lattice distortions, which have a strong scattering effect on electrons and phonons, significantly reducing the thermal conductivity of the joint [41]. Thus, the dissolution and precipitation of the secondary phases change the solute atom content in the ZM51 alloy, significantly impacting the thermal conductivity. The amount of α-Mn phases in the SZ is much lower than that in the BM (as shown in Fig. 4), indicating that α-Mn phases have dissolved during the welding process. The dissolution of α-Mn phases means an increase in Mn atoms in the Mg matrix, leading to a reduced thermal conductivity in the SZ. Although α-Mn phases dissolved in the HAZ, increasing the Mn content, the subsequent precipitation of β_1' and β_2' phases decreased the Mg and Zn contents in the matrix. Paradoxically, the reduction in Mg and Zn increased the thermal conductivity. Secondly, grain size is another crucial factor influencing thermal conductivity variations. This is primarily because grain boundaries impede the motion of electrons and phonons capable of heat transfer, thereby reducing thermal conductivity. Compared to the BM, the SZ exhibits a decreased average grain size, which consequently lowers its thermal conductivity. In contrast, the HAZ, which has a larger average grain size, exhibits improved thermal conductivity. This observation aligns with others' findings [44,45]. Finally, the weakening of the basal texture contributes to the improvement in thermal

conductivity [46]. During the FSW process of ZM51 alloy, the ⟨0001⟩ basal plane texture in SZ tends to deflect towards the ND, strengthening the texture along that axis. This results in a denser lattice along the ND, reducing the average free travel of heat transfer electrons and phonons, thereby decreasing the thermal conductivity of SZ.

4.2.2 FSW+AG joint

After AG, the thermal conductivity in all regions of the ZM51 alloy joint exceeded 120 W/(m·K), not only enhancing the thermal performance but also achieving a more uniform distribution of thermal conductivity across the joint. In BM, SZ, and HAZ of the FSW+AG joints, the average grain size increased by 25.0, 7.0, and 2.0 μm (Fig. 5), respectively, leading to respective improvements of 13.1, 16.6, and 8.0 W/(m·K) in thermal conductivity (Fig. 14). Despite negligible changes in average grain size in HAZ, thermal conductivity increased by 7%, indicating that factors beyond grain size significantly influence thermal conductivity. Similarly, there were no significant changes in the texture of the FSW+AG joint compared to that of the FSW joint. The most notable difference at the microstructural level between FSW+AG and FSW joints is the substantial precipitation of β_1' and β_2' phases in all regions of the joints, with a relatively uniform distribution. This resulted in the significant consumption of Zn and Mg atoms within the matrix, reducing the scattering effect of solute atoms on electrons and phonons, thereby facilitating the long-distance motion of heat transfer phonons [47] and significantly enhancing thermal conductivity. SHI et al [48] also found that in cast $Mg_{92}Zn_4Y_4$ and $Mg_{92}Zn_4Y_3Gd_1$ alloys, the precipitation of *W* phase ($Mg_3Zn_3Y_2$) led to an increase in thermal conductivity.

Consequently, the primary factor for the enhanced thermal conductivity and its progression towards uniformity in AG-treated joints can be largely attributed to the impact of solute atoms. The significant improvement resulting from the precipitation phase outweighs the effects of grain size and texture strength on thermal conductivity.

5 Conclusions

(1) The microhardness, UTS, and YS of the FSW+AG joint reached 98%, 88%, and 94% those of BM, respectively. The thermal conductivity of the SZ and HAZ in the joint achieved 112% and 113% that of BM, respectively, demonstrating a balance between mechanical properties and thermal conductivity.

(2) After the FSW+AG treatment, the grain sizes in the SZ, TMAZ and HAZ were 16, 17 and 78 μm, respectively. Notably, this treatment led to the significant emergence of β_1' and β_2' phases within the SZ and TMAZ, while exclusively β_2' phase precipitated in the HAZ. Precipitation strengthening increased the joint's microhardness by 22% and the YS by 69%.

(3) Both FSW and FSW+AG joints fractured within the TMAZ. This is attributed to the increased susceptibility of the TMAZ to $\{0001\}\langle 11\bar{2}0\rangle$ basal plane slip, and $60°\langle 10\bar{1}0\rangle$ and $86°\langle 11\bar{2}0\rangle$ twinning, resulting in stress concentration and fracture within this zone during tensile loading.

(4) Compared to the BM, the FSW joint exhibited lower thermal conductivity due to the dissolution of precipitate phases, grain refinement, and enhanced basal plane texture. In contrast, the FSW+AG joint showed improved and more uniform thermal conductivity, stemming from the precipitation of β_1' and β_2' phases, which reduced the solute atom content.

CRediT authorship contribution statement

Xu ZHANG: Investigation, Characterization, Data interpretation, Visualization, Validation, Writing − Original draft, Writing − Review & editing; **Zhi WANG:** Writing − Original draft, Data curation, Visualization, Validation; **Feng-ming QIANG:** Investigation, Methodology, Writing − Original draft; **Wen WANG:** Resources, Funding acquisition, Writing − Review & editing; **Peng HAN:** Conceptualization, Writing − Review & editing; **Ting ZHANG:** Supervision, Writing − Review & editing; **Qiang LIU:** Project administration; **Yi LIU:** Supervision; **Ke-yue HUO:** Validation; **Kuai-she WANG:** Funding acquisition; **Ke QIAO:** Project administration.

Declaration of competing interest

The authors declare that they have no known competing financial interests or personal relationships that could have appeared to influence the work reported in this paper.

Acknowledgments

This work was supported by the Key Research and

Development Program of Shaanxi Province, China (No. 2017ZDXM-GY-037), the National Natural Science Fund for Excellent Young Scholars, China (No. 52222410), the National Natural Science Foundation of China (Key Program) (No. 52034005), the National Natural Science Foundation of China (No. 52227807), the National Key Research and Development Program of China (No. 2021YFB3700902), and the Shaanxi Province Qinchuangyuan "Scientist + Engineer" Team Program, China (No. 2022KXJ-072).

References

[1] LIU Zhan, NIE Jin-feng, ZHAO Yong-hao. Effect of deformation processing on microstructure evolution and mechanical properties of Mg−Li alloys: A review [J]. Transactions of Nonferrous Metals Society of China, 2024, 34(1): 1−25.

[2] ZHANG Ye, HU Yue-hua, WANG Li, SUN Wei. Mg recovery from salt lake brine into forsterite refractory materials via precipitation−calcination process [J]. Transactions of Nonferrous Metals Society of China, 2024, 34(2): 694−708.

[3] DARENFAD W, GUERMAT N, MIROUH K. Thoughtful investigation of ZnO doped Mg and co-doped Mg/Mn, Mg/Mn/F thin films: A first study [J]. Journal of Molecular Structure, 2023, 1286: 135574.

[4] LIU Lin, YU Si-rong, WANG Bing-ying, ZHU Guang, LIU En-yang. Effects of heat treatment on mechanical properties and degradation behavior of hollow glass microsphere reinforced Mg−15Al−5Zn−1.5Cu composites [J]. Transactions of Nonferrous Metals Society of China, 2023, 33(9): 2613−2630.

[5] WANG Lyu-yuan, HUANG Jian, PENG Yong, WU Yi-xiong. Precipitates evolution in the heat affected zone of Mg−Gd−Y−Zr alloy in T6 condition during laser welding [J]. Materials Characterization, 2019, 154: 386−394.

[6] YU Zhao-hui, YAN Hong-ge, YIN Xu-yu, LI Ying, YAN Guo-hua. Liquation cracking in laser beam welded joint of ZK60 magnesium alloy [J]. Transactions of Nonferrous Metals Society of China, 2012, 22(12): 2891−2897.

[7] ZHANG Yu, LI Hong, LI Zhuo-xin. The role of liquid feeding in nugget-edge cracking in resistance spot welding of dissimilar magnesium alloys [J]. Journal of Materials Research and Technology, 2021, 12: 788−795.

[8] GAO Xiao-bo, GAO Tian-yi, QIU Ran-feng, IWAMOTO C, SATONAKA S. Microstructure of $Mg_{96}Zn_2Y_2$ alloy joint formed by resistance spot welding [J]. Materials Research Express, 2019, 6(11): 1165a5.

[9] ZHANG Guo-qing, TONG Xin, WU Guo-hua, ZHANG Liang, SUI Huai-ming, ZHANG Xiao-long. Research on the post-weld heat treatment of TIG repair welded joint of sand-cast Mg−Y−Re−Zr alloy [J]. Materials Science and Engineering: A, 2021, 821: 141577.

[10] POURANVARI M. Critical review on fusion welding of magnesium alloys: Metallurgical challenges and opportunities [J]. Science and Technology of Welding and Joining, 2021, 26: 559−580.

[11] ZHAO Wan-jun, JIAO Qing-jie, CHEN Peng-wan, YAN Shi, ZHU Yan-li, ZHANG Bi, ZENG Xin, LIU Da-zhi, OU Yan-peng, WANG Fang. Synergetic energetic kinetics of Mg−Zn alloys and pyrotechnics [J]. Combustion and Flame, 2022, 240: 112000.

[12] LIU Qiang, WANG Wen, PENG Pai, ZHANG Ting, HAN Peng, GUAN Xiao-hu, WANG Zhi, QIAO Ke, CAI Jun, WANG Kuai-she. Microstructure evolution and strengthening mechanism of friction stir welded joint of 20 mm-thick AZ31 magnesium alloy [J]. Transactions of Nonferrous Metals Society of China, 2023, 33(11): 3295−3308.

[13] QIAO Ke, WANG Kuai-she, WANG Jia, HAO Zheng-yang, XIANG Ya-ting, HAN Peng, CAI Jun, YANG Qi, WANG Wen. Microstructural evolution and deformation behavior of friction stir welded twin-induced plasticity steel [J]. Journal of Materials Science & Technology, 2024, 169: 68−81.

[14] XU Nan, ZHANG Wei-da, CAI Si-qi, ZHUO Yue, SONG Qi-ning, BAO Ye-feng. Microstructure and tensile properties of rapid-cooling friction-stir-welded AZ31B Mg alloy along thickness direction [J]. Transactions of Nonferrous Metals Society of China, 2020, 30(12): 3254−3262.

[15] WANG Hong-duo, ZHOU Zhi-yong, WANG Kuai-she, WANG Wen, HAN Peng, ZHANG Cheng-wen, LU Yong-xin, LI Guang, LU Yi-di, LI Xiao, LIU Yan-ming, ZHANG Xiao-yong. Microstructure and corrosion behaviors of friction stir-welded Q235 low-carbon steel joint [J]. Journal of Iron and Steel Research International, 2023, 30(12): 2517−2530.

[16] XU Nan, FENG Ruo-nan, REN Zi-ke, GU Bo-kun, SONG Qi-ning, BAO Ye-feng. Improvement of microstructure and mechanical properties of AZ61 Mg alloys subjected to rapid cooling friction stir welding [J]. Science and Technology of Welding and Joining, 2021, 26(7): 503−512.

[17] MOIDUDDIN K, SIDDIQUEE A N, ABIDI M H, MIAN S H, MOHAMMED M K. Friction stir welding of thick plates of 4Y3Gd Mg alloy: An investigation of microstructure and mechanical properties [J]. Materials, 2021, 14(22): 6924.

[18] XU Nan, FENG Ruo-nan, SONG Qi-ning, ZHAO Jian-hua, BAO Ye-feng. Influence of heterogeneous microstructures on the mechanical properties of low-temperature friction stir processed AZ91D Mg alloy [J]. Materials Science and Engineering: A, 2021, 809: 141004.

[19] LI Lian-hui, CAO Hong-shuai, QI Fu-gang, WANG Qing, ZHAO Nie, LIU Ying-du, YE Xue, OUYANG Xiao-ping. Effect of heat treatment on microstructure and mechanical properties of Mg−5Zn−1Mn alloy tube [J]. Metals, 2020, 10(3): 301.

[20] BAZHENOV V E, KOLTYGIN A V, SUNG M C, PARK S H, TSELOVALNIK Y V, STEPASHKIN A A, RIZHSKY A A, BELOV M V, BELOV V D, MALYUTIN K V. Development of Mg−Zn−Y−Zr casting magnesium alloy with high thermal conductivity [J]. Journal of Magnesium and Alloys, 2021, 9(5): 1567−1577.

[21] ZHOU You, SUN Lin-ping, DING Mei-ling, BAO N, WU Xiao-xiao, NARSU B. Chemical-structural coupling in magnesium−scandium alloys [J]. Results in Physics, 2023, 50: 106582.

[22] ZHONG Li-ping, WANG Yong-jian, LUO Hong, LUO Chang-sen, PENG Jian. Evolution of the microstructure, texture and thermal conductivity of as-extruded ZM60 magnesium alloy in pre-compression [J]. Journal of Alloys and Compounds, 2019, 775: 707−713.

[23] YAMASAKI M, KAWAMURA Y. Thermal diffusivity and thermal conductivity of Mg−Zn-rare earth element alloys with long-period stacking ordered phase [J]. Scripta Materialia, 2009, 60(4): 264−267.

[24] GAO Shi-kang, ZHAO Hong-yun, LI Gao-hui, MA Ling-hang, ZHOU Li, ZENG Ru-chuan, LI Dong-xiao. Microstructure, properties and natural ageing behavior of friction stir welded dual-phase Mg−Li alloy [J]. Journal of Materials Processing Technology, 2024, 324: 118252.

[25] YANG Xia-wei, MENG Ting-xi, CHU Qiang, SU Yu, GUO Zhen-guo, XU Rui, FAN Wen-long, MA Tie-jun, LI Wen-ya. A review on linear friction welding of Ni-based superalloys [J]. International Journal of Minerals, Metallurgy and Materials, 2024, 31(6): 1382−1391.

[26] GUO Zhen-guo, MA Tie-jun, YANG Xia-wei, LI Ju, LI Wen-ya, VAIRIS A. Multi-scale analyses of phase transformation mechanisms and hardness in linear friction welded $Ti_{17}(\alpha+\beta)/Ti_{17}(\beta)$ dissimilar titanium alloy joint [J]. Chinese Journal of Aeronautics, 2024, 37(1): 312−324.

[27] XIN Ren-long, LIU De-jia, SHU Xiap-gang, LI Bo, YANG Xiao-fang, LIU Qing. Influence of welding parameter on texture distribution and plastic deformation behavior of as-rolled AZ31 Mg alloys [J]. Journal of Alloys and Compounds, 2016, 670: 64−71.

[28] SHANG Q, NI D R, XUE P, XIAO B L, MA Z Y. Evolution of local texture and its effect on mechanical properties and fracture behavior of friction stir welded joint of extruded Mg−3A1−1Zn alloy [J]. Materials Characterization, 2017, 128: 14−22.

[29] WANG Qing-hang, ZHAI Hao-wei, LIU Lin-tao, XIA Hong-bo, JIANG Bin, ZHAO Jun, CHEN Da-lun, PAN Fu-sheng. Novel Mg−Bi−Mn wrought alloys: The effects of extrusion temperature and Mn addition on their microstructures and mechanical properties [J]. Journal of Magnesium and Alloys, 2022, 10(9): 2588−2606.

[30] WU Qin, YAN Hong-ge, CHEN Ji-hua, XIA Wei-jun, SONG Min, SU Bin. Dynamic precipitation behavior before dynamic recrystallization in a Mg−Zn−Mn alloy during hot compression [J]. Materials Characterization, 2019, 153: 14−23.

[31] LIU Yu-xuan, LI Yang-xin, ZHANG Huan, ZHU Qing-chun, QI Xi-xi, WANG Jie, WANG Jin-hui, JIN Pei-peng, ZENG Xiao-qin. Influence of twinning-induced recrystallization on texture evolution in a high strain rate compressed Mg−Zn alloy [J]. Materials Characterization, 2020, 162: 110192.

[32] LI G H, ZHOU L, ZHANG H F, GUO G Z, LUO S F, GUO N. Evolution of grain structure, texture and mechanical properties of a Mg−Zn−Zr alloy in bobbin friction stir welding [J]. Materials Science and Engineering: A, 2021, 799: 140267.

[33] MU S J, JONAS J J, GOTTSTEIN G. Variant selection of primary, secondary and tertiary twins in a deformed Mg alloy [J]. Acta Materialia, 2012, 60(5): 2043−2053.

[34] TAN Li, ZHANG Xi-yan, XIA Ting, SUN Qi, HUANG Guang-jie, XIN Ren-long, LIU Qing. $\{10\bar{1}2\}-\{10\bar{1}2\}$ double tensile twinning in a Mg−3Al−1Zn alloy sheet during cyclic deformation[J]. Materials Science and Engineering: A, 2018, 711: 205−211.

[35] KWEON S, RAJA D S. Investigation of the mechanical response of single crystal magnesium considering slip and twin [J]. International Journal of Plasticity, 2019, 112: 1−17.

[36] XIN Ren-long, LI Bo, LIAO Ai-lin, ZHOU Zheng, LIU Qing. Correlation between texture variation and transverse tensile behavior of friction-stir-processed AZ31 Mg alloy [J]. Metallurgical and Materials Transactions a-Physical Metallurgy and Materials Science, 2012, 43(7): 2500−2508.

[37] ZHANG Jun-lei, HUANG Guang-sheng, LIU Shuai-shuai, XIE Yu-lu, WANG Guan-gang, JIANG Bin, TANG Ai-tao, PAN Fu-sheng. Microstructure evolution and mechanical properties of friction stir welded dissimilar joints of as-extruded AM60 and AZ31 alloys [J]. Materials Science and Engineering: A, 2019, 759: 479−489.

[38] HUSSER E, BARGMANN S. Modeling twinning-induced lattice reorientation and slip-in-twin deformation [J]. Journal of the Mechanics and Physics of Solids, 2019, 122: 315−339.

[39] ZHANG Zhen-yan, PENG Li-ming, ZENG Xiao-qin, DING Wen-jiang. Effects of Cu and Mn on mechanical properties and damping capacity of Mg−Cu−Mn alloy [J]. Transactions of Nonferrous Metals Society of China, 2008, 18(Supple.): 55−58.

[40] FIGUEIREDO R B, LANGDON T G. Deformation mechanisms in ultrafine-grained metals with an emphasis on the Hall−Petch relationship and strain rate sensitivity [J]. Journal of Materials Research and Technology, 2021, 14: 137−159.

[41] LI Gao-hui, CHEN Ting, FU Bang-long, SHEN Jun-jun, BERGMANN L, ZHOU Li, CHEN Ke, DOSSANTOS J F, KLUSEMANN B. Semi-stationary shoulder bobbin-tool: A new approach in tailoring macrostructure and mechanical properties of bobbin-tool friction stir welds in magnesium alloy [J]. Journal of Materials Processing Technology, 2023, 317: 117984.

[42] ZHANG Ding-fei, SHI Guo-liang, DAI Qing-wei, YUAN Wei, DUAN Hong-ling. Microstructures and mechanical properties of high strength Mg−Zn−Mn alloy [J]. Transactions of Nonferrous Metals Society of China, 2008, 18(Supple.): 59−63.

[43] HU Ling-fei, GU Qin-fei, LI Qian, ZHANG Jie-yu, WU Guang-xin. Effect of extrusion temperature on microstructure, thermal conductivity and mechanical properties of a Mg−Ce−Zn−Zr alloy [J]. Journal of Alloys and Compounds, 2018, 741: 1222−1228.

[44] YING T, ZHENG M Y, LI Z T, QIAO X G. Thermal conductivity of as-cast and as-extruded binary Mg−Al alloys [J]. Journal of Alloys and Compounds, 2014, 608: 19−24.

[45] HE Jia-le, CHEN Ji-hua, YAN Hong-ge, XIA Wei-jun, SU Bin, SUN You-ping, NIE Yang, HUANG Wen-sen, WU Mou-xin. Effects of Zn/Ga ratio on microstructure, mechanical, damping and thermal properties of Mg−Zn−Ga alloy solid solutions [J]. Journal of Materials Research, 2022, 37(10): 1727−1738.

[46] SU Chuang-ye, LI De-jiang, LUO A A, YING Tao, ZENG Xiao-qin. Effect of solute atoms and second phases on the

thermal conductivity of Mg−RE alloys: A quantitative study [J]. Journal of Alloys and Compounds, 2018, 747: 431−437.
[47] HUANG Dan-dan, LIU Shu-hong, XU Hong-hui, DU Yong. Phase equilibria of the Mg−Mn−Zn system at 593 K (320 °C) [J]. Journal of Alloys and Compounds, 2016, 688: 1115−1124.
[48] SHI Fei, WANG Chun-qing, GUO Xue-feng. Microstructures and properties of as-cast $Mg_{92}Zn_4Y_4$ and $Mg_{92}Zn_4Y_3Gd_1$ alloys with LPSO phase [J]. Rare Metal Materials and Engineering, 2015, 44(7): 1617−1622.

搅拌摩擦焊接和时效处理制备高强度、高热导率的 ZM51 镁合金接头

张 旭[1,2]，王 智[1,2]，强凤鸣[1,2]，王 文[1,2]，韩 鹏[1,2]，
张 婷[1,2]，刘 强[1,2]，刘 艺[1,2]，霍可越[1,2]，王快社[1,2]，乔 柯[1,2]

1. 西安建筑科技大学 冶金工程学院，西安 710055；
2. 功能材料加工国家与地方联合工程研究中心，西安 710055

摘 要：采用搅拌摩擦焊接(FSW)和时效热处理(AG)制备了具有高强度、高热导率的 ZM51 镁合金接头。在 FSW 过程中，热影响区(HAZ)生成了 β_1' 相和 β_2' 相，而搅拌区(SZ)和热机械影响区(TMAZ)无新相生成。AG 后，大量 β_1' 相和 β_2' 相在 SZ 和 TMAZ 中析出，而 HAZ 中仅有 β_2' 相析出。由于析出强化作用，接头的平均显微硬度、屈服强度和极限抗拉强度分别达到母材(BM)的 98%、94%和 88%。值得注意的是，TMAZ 更容易发生 $\{0001\}\langle 11\bar{2}0\rangle$ 基面滑移和 $60°/\langle 10\bar{1}0\rangle$ 及 $86°/\langle 11\bar{2}0\rangle$ 孪生，导致接头断裂于 TMAZ。此外，β_1' 相和 β_2' 相的析出提升了接头的热导率，平均热导率为 121.7 W/(m·K)，达到 BM 的 112%。

关键词：搅拌摩擦焊；ZM51 镁合金；析出相；拉伸性能；热导率

(Edited by Wei-ping CHEN)